INSTITUTE OF PHYSICS PUBLISHING MODELLING AND SIMULATION IN MATERIALS SCIENCE AND ENGINEERING

Modelling Simul. Mater. Sci. Eng. **14** (2006) 1409–1420 doi:10.1088/0965-0393/14/8/008

Molecular dynamics simulations of crack propagation in Ni with defects

Majid Karimi[1], **Tom Roarty**[1] **and Theodore Kaplan**[2]

[1] Physics Department, Indiana University of Pennsylvania, Indiana, PA 15705, USA
[2] Computer Science and Mathematics Division, Oak Ridge National Laboratory, Oak Ridge, TN 37831, USA

Received 11 June 2006, in final form 26 October 2006
Published 27 November 2006
Online at stacks.iop.org/MSMSE/14/1409

Abstract
A series of molecular dynamics simulations using the embedded atom method is conducted to investigate crack propagation under mode I loading in a Ni single crystal with and without defects. The crack system (0 0 1)[1 0 0] in a slab of 160 000 atoms was studied. Defects consisting of lines of vacancies were introduced near the crack tip. Critical loads and strain energy distributions around the crack tip are obtained. Our results indicate that the critical strain necessary for crack propagation is dependent on the defect configuration and can either increase or decrease relative to the defect-free system.

1. Introduction

The study of crack propagation in materials can be very difficult due to its multiscale nature. The smallest scale is the breaking of the bonds between atoms as the crack propagates. The driving force behind the bond breaking is the far strain field due to the loading applied to the sample. The strain field is influenced by micro-cracks, sample geometry and size, as well as dislocations and other defects. It is understood that propagation of a crack in a material not only depends on the load but also on the various types of defects present. Because a material fails when the strain concentration exceeds the failure strength of materials, failure analyses is directly related to the strain concentration near the crack tip. Modelling of crack propagation is traditionally done using a continuum mechanics approach in which the effects of atomic scale defects are not included. Most of the simulations of brittle crack propagation in the presence of defects were performed in either two-dimensional or otherwise three-dimensional systems with less degrees of freedom [1]. The experimental study of atomic scale defects and their effects on toughness of materials were done in copper in the presence of a grain boundary [2]. With the advent of more efficient hardware and software it is now possible to model crack propagation in a solid material in the presence of defects from an atomistic standpoint.

A logical approach to the study of brittle crack propagation is to examine an experimentally brittle material such as a semiconductor or a bcc transition metal. Due to the complexity of bonding in these materials, fast and reliable interatomic potentials are rarely available.

On the other hand, fast and quite reliable interatomic potential models are available for nickel and other fcc metals. Although fcc metals, in general, and nickel, in particular, are known as ductile materials, the study of brittle crack propagation in these materials is still possible for the specific crack system that is employed here in crystalline nickel.

There are several types of classical atomistic computer simulations available for modelling the process of crack propagation in a solid material. They include molecular dynamics (MD), Monte-Carlo and molecular statics (MS). Among these three frequently used methods, MD and MS are best suited for this application. While MD can provide time-dependent information necessary for the calculation of crack speed, MS is best suited for the calculation of the strain energy distribution near the crack tip.

The main objective of this paper is to study the effect of defects on crack propagation. We begin by examining crack propagation in the defect-free crystal for the Ni EAM interatomic potential we have chosen. Once the crack behaviour of the defect-free lattice is described, defects consisting of lines of vacancies are inserted into the lattice near the crack tip and the critical energy release rate and strain energy distributions near the crack tip are evaluated and analysed. By examining the change in strain energy due to the introduction of defects for each atom near the crack tip, one can gain a better understanding of the fracture process in defective systems.

The paper is organized as follows. A brief summary of the embedded atom method (EAM) employed in this work is presented in section 2.1. The crack geometry as well as the formulae involved in the calculation of the Griffith's energy function G are presented in section 2.2. A brief description of MD as well as its application to the present case is given in section 2.3. Results are presented and discussed in section 3.1 for the defect-free crystal and in 3.2 for the crystal with defects. Finally, the concluding remarks are given in section 4.

2. Computational procedure

2.1. Embedded atom method

The EAM was originally developed by Daw and Baskes as a model for the bonding of fcc metals and subsequently has been extended by Baskes to other crystalline structures [3]. The EAM potential consists of a many body term representing the interaction of an embedding atom core with the electronic charge density of the remaining atoms in the system and a pair wise term representing the electrostatic interactions between the atoms cores. The many body term is referred to as the embedding function. The total energy E of a system of N atoms can be written as

$$E_i = F_i(\rho_i) + \frac{1}{2}\sum_{j\neq i}\phi_{ij}(r_{ij}), \tag{1.1}$$

$$E_{\text{pot}} = \sum_{i=1}^{N} E_i, \tag{1.2}$$

$$\rho_i = \sum_{j\neq i}\rho_{ij}^{a}(r_{ij}), \tag{1.3}$$

where E_i is the energy of atom i, F_i is the embedding energy of atom i, ρ_i is the electron density at site i, ϕ_{ij} is the pair potential function between atoms i and j and ρ_{ij}^{a} is the atomic charge density of atom j at the location of atom i. The embedding energy and pair potential functions were determined, originally, by considering functional forms for them and fitting to the bulk experimental data.

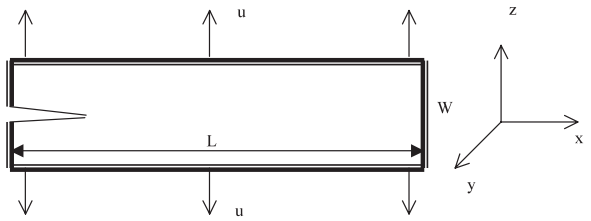

Figure 1. Schematic of the crack propagation geometry under mode I (tensile strain) loading.

The EAM functions for nickel employed here are the ones that were recently developed by Mishin *et al* [4] and are believed to be superior to the previous EAM functions due to the fact that they are fitted to a richer database using a new fitting scheme. Mishin EAM functions are fitted to the elastic constants, surface energies as well as to other bulk and surface data. For the present application it is critical that the potential reproduces the elastic constants as well as surface energies very accurately.

2.2. *Crack geometry*

A crack is introduced into the lattice by partially turning off interatomic bonds between atoms in eight consecutive (0 0 1) planes. The two middle planes are the upper and lower surfaces of the starter crack. This restriction on the potential prevents the initial crack from rebonding. Following the prescription set forth in [5] for a similar Ni EAM potential, the length of the starter crack is set to roughly $L/4$, where L is the total length of the slab along the x-direction. For the (0 0 1)[1 0 0] crack system, the crack-free surfaces are (0 0 1) and the crack propagates along the [1 0 0] direction, as shown in figure 1. The computational cell is periodic along $y = [0\,1\,0]$ and an external tensile load is applied along the $z = [0\,0\,1]$ direction by expanding the lattice along the z-direction and freezing the upper and lower free surfaces along that direction. The periodic boundary condition along the y-direction emulates the plane strain regime and is believed to prevent emission of dislocations in the crystal [5]. This in turn makes it possible to study brittle crack propagation in a material that is originally ductile. We checked the size dependences of our results and concluded that a sample size of about $702 \times 12.3 \times 174\ \text{Å}^3$ with 160 000 atoms was sufficiently large to take care of the long-range character of the crack strain fields.

The strain energy release rate G is an important quantity in the study of crack propagation. According to Griffith's criteria, a brittle crack under mode I loading will propagate when G corresponding to an applied load becomes equal or greater than $2\gamma_s$, where γ_s is the surface energy of each plane of the crack. Even though Griffith's formula is a simple way of predicting the critical value of G for the crack propagation, its usefulness is limited in that it only provides a lower bound of G. In the loading configuration of figure 1, G is the strain energy per unit area of (0 0 1) plane in front of the crack tip. A more realistic way of calculating G is based on the strained energy release from a strained rectangular prism of sides $x = L$, $y = y$ and $z = W$. For mode I loading, the strain energy density stored in the slab of figure 1 has a simple form,

$$U = \frac{1}{2}E'\varepsilon^2 = \frac{1}{2}\frac{E}{1-\nu^2}\varepsilon^2, \tag{2}$$

where U is the strain energy density, E' is the effective Young's modulus, ε is the applied strain and for plane strain condition $E' = E/(1-\nu^2)$, where E is Young's modulus and ν is Poisson's ratio. The energy release rate G is defined as the elastic energy released per unit

length advance of the crack tip [6],

$$G = U \times W = \frac{1}{2}\frac{EW}{1-\nu^2}\varepsilon^2. \tag{3}$$

Isotropic Young's modulus, E, and Poisson's ratio, ν, can be approximated from the exact elastic constants C_{11}, C_{12} and C_{44} using the Voigt averaging method [6],

$$\mu = C_{44}, \tag{4.1}$$
$$\lambda = C_{12}, \tag{4.2}$$
$$\nu = \lambda/(2(\lambda+\mu)), \tag{4.3}$$
$$E = 2\mu(1+\nu), \tag{4.4}$$

where C_{12} and C_{44} are reported in [4] for the nickel EAM potential employed here.

The dynamic fracture toughness, G_d, is related to the crack speed, v, using the continuum mechanical solution [6–8]:

$$G_\mathrm{d} = G_\mathrm{s}(1 - v/v_\mathrm{R}), \tag{5}$$

where G_s is the static strain energy release rate and v_R is the Rayleigh wave speed in the direction of crack propagation. G_d is the part of G_s that goes into creating the crack surfaces as well as dislocations and other types of lattice defects. Prediction of continuum mechanics for v/v_R versus G_s can be obtained by inverting equation (5):

$$v/v_\mathrm{R} = (G_\mathrm{s} - G_\mathrm{d})/G_\mathrm{s}, \tag{6}$$

where G_d is approximated with the Griffith load, $G_\mathrm{d} = 2\gamma_\mathrm{s}$. There are three limiting speeds when sound wave propagates inside a solid. In the order of increasing velocity they are Rayleigh (v_R), shear (v_2) and longitudinal (v_1). Using formulae for v_1 and v_2, given after equation (8), and $C_{11} = 247$ GPa, $C_{44} = 125$ GPa and $\rho = 8900\,\mathrm{kg\,m^{-3}}$ from the interatomic potential, the values of $v_1 = 5268\,\mathrm{m\,s^{-1}}$ and $v_2 = 3748\,\mathrm{m\,s^{-1}}$ are obtained. The Rayleigh wave is a wave that propagates over a surface in a specific direction. In the present situation, the Rayleigh wave propagates over a (0 0 1) plane in the [1 0 0] direction and the following equation was developed [9] for that situation,

$$C_{11}(\rho v_\mathrm{R}^2 - C_{44})\left(\rho v_\mathrm{R}^2 - \left(C_{11} - \frac{C_{12}^2}{C_{11}}\right)\right)^2 = C_{44}(\rho v_\mathrm{R}^2 - C_{11})(\rho v_\mathrm{R}^2)^2. \tag{7}$$

Equation (7) is solved, numerically, using Mathematica [10] for a nonzero real solution $v_\mathrm{R} = 2797\,\mathrm{m\,s^{-1}}$ that is less than v_2 and v_1. Equation (7) reduces to the well-known Rayleigh wave speed in an isotropic material [11] such as a polycrystalline medium when $C_{44} = 0.5(C_{11} - C_{12})$,

$$v_\mathrm{R}^6 - \frac{4(C_{11}-C_{12})}{\rho}v_\mathrm{R}^4 + \frac{2(C_{11}-C_{12})^2}{\rho^2}\left(3 - \frac{C_{11}-C_{12}}{C_{11}}\right)v_\mathrm{R}^2 + \frac{(C_{11}-C_{12})^3}{\rho^3}\left(\frac{C_{11}-C_{12}}{C_{11}} - 2\right)$$
$$= \left(\frac{v_\mathrm{R}}{v_2}\right)^6 - 8\left(\frac{v_\mathrm{R}}{v_2}\right)^4 + \left(\frac{24}{v_2^2} - \frac{16}{v_1^2}\right)v_\mathrm{R}^2 - 16\left(1 - \frac{v_2^2}{v_1^2}\right) = 0, \tag{8}$$

where $v_1 = \sqrt{C_{11}/\rho}$ and $v_2 = \sqrt{C_{44}/\rho} = \sqrt{(0.5(C_{11} - C_{12}))/\rho}$. Equation (8) is solved using mathematica and a positive, real root $v_\mathrm{R} = 2172\,\mathrm{m\,s^{-1}}$ is obtained. In the literature [12], the solution of equation (8) is quite often written as

$$v_\mathrm{R} = \eta v_2 = ((0.862 + 1.14\nu)/(1+\nu))v_2. \tag{9}$$

2.3. MD calculation

The atomistic computer simulation that is employed here is based on the classical MD method. The input to any MD is a lattice file with positions and velocities of all the atoms in the system at time zero. In the MD simulation, Newton's equations of motion are integrated using a numerical algorithm (Nordsik algorithm in our case [13]) to obtain the phase space trajectories of all atoms in the system using a force function that is derived from a model potential E_{pot}. For a general discussion of MD, we refer the reader to the book by Allen and Tildesley [14]. The simulations reported in this paper employ an fcc lattice of Ni with 160 000 atoms for the defect-free system. Newton's second law when applied to atom i has the following form,

$$f_i = m_i a_i = m_i \frac{\mathrm{d}v_i}{\mathrm{d}t} = \frac{\mathrm{d}^2 r_i}{\mathrm{d}t^2}, \tag{10.1}$$

$$f_i = -\frac{\partial E_{\mathrm{pot}}}{\partial x_i}, \tag{10.2}$$

where E_{pot} is the total potential energy from equation (1.1). Numerical solutions of equation (10.1) for N atoms in the system would lead to $3N$ equations for the positions and $3N$ equations for the velocities of all the atoms in the system at each time step from their values at the previous time step. To obtain values of positions and velocities of atoms at time $\mathrm{d}t$ we need to have their values at time zero. Values of positions of atoms from their perfect fcc crystalline site were used as their initial values at time zero. The initial values of the velocities were set to zero.

The calculation is performed in the canonical ensemble using a viscous damping temperature control presented in [15]. In this part, we summarize the highlights of the method that is believed to be very effective in absorbing the strain waves emitted from the crack tip [5]. A damping force $\boldsymbol{F}_i = -\xi \boldsymbol{v}_i$ is applied to atom i which in turn causes a rate of change in its thermal energy by $\boldsymbol{F}_i \cdot \boldsymbol{v}_i = -\xi \boldsymbol{v}_i \cdot \boldsymbol{v}_i = (\partial/\partial t)(3k_{\mathrm{B}}T_i) = 3k_{\mathrm{B}}\,\mathrm{d}T_i/\mathrm{d}t$. The rate of cooling of atom i can also be described using the following differential equation $\mathrm{d}T_i/\mathrm{d}t = -\alpha(T_i - T_{\mathrm{d}})$, where $\tau = 1/\alpha$ is the time constant of cooling of atom i and T_{d} is its desired temperature. Substituting $\mathrm{d}T_i/\mathrm{d}t$ from the second equation above into the first equation leads to the $-\xi \boldsymbol{v}_i \cdot \boldsymbol{v}_i = -3k_{\mathrm{B}}\alpha(T_i - T_{\mathrm{d}})$, where $T_i = mv_i^2/(3k_{\mathrm{B}})$ and m are the actual temperature and mass of atom i. Using the last equation for T_i we can then write the following equation for $\xi = \alpha m(T_i - T_{\mathrm{d}})/T_i$. In order to avoid the singularity at $T_i = 0$, a small number is added to the denominator of equation for ξ. The sample is divided into two parts: skin depth and the inner part. Skin depth, in figure 1, is represented by a black band near the boundary of the sample. The ramped viscous damping is applied to all four (top, bottom, right, left) regions. In the inner part, fixed values of $T_{\mathrm{d}} = 10\,\mathrm{K}$ and $\alpha m = 7.98 \times 10^{-13}\,\mathrm{kg\,s^{-1}}$ ($\alpha = 8.2 \times 10^{12}\,\mathrm{s^{-1}} = 8.2\,(\mathrm{ps})^{-1}$) [15] are employed to control the temperature. In the skin depth region, α and T_{d} are ramped from their values at the inner boundary (α_1 and T_{d1}) to those at the outer boundary (α_2 and T_{d2}) of the skin depth region. In the MD simulations reported here, $\alpha_1 = 8.2\,(\mathrm{ps})^{-1}$, $T_{\mathrm{d1}} = 10\,\mathrm{K}$, $\alpha_2 = 2\omega_{\mathrm{E}}\,(\mathrm{ps})^{-1}$, $T_{\mathrm{d2}} = 0\,\mathrm{K}$, where ps stands for pico-second. The skin depth region has a width of approximately 30 Å when the sample is not under strain. It was suggested [5] that a maximum damping coefficient $\alpha_2 = 2\omega_{\mathrm{E}}$ is sufficient to critically damp sound waves at $T_{\mathrm{d2}} = 0$. The Einstein frequency is determined using an approximate formula $\omega_{\mathrm{E}} = 2N_0^{1/3}E^{1/2}/(\rho^{1/6}M^{1/3})$ presented in [16], where N_0 is the Avogadro number, ρ is the density, M is the atomic mass unit and E is Young's modulus. Using the formulae above, we find $\alpha_2 = 93.4\,(\mathrm{ps})^{-1}$ and an Einstein frequency of $46.7\,(\mathrm{ps})^{-1}$.

For most of the simulations a time step of $\mathrm{d}t = 0.001\,\mathrm{ps}$ was employed for a total run time of 40 ps or 40,000 time step. For some of the simulations $\mathrm{d}t$ was increased to 0.0015 ps

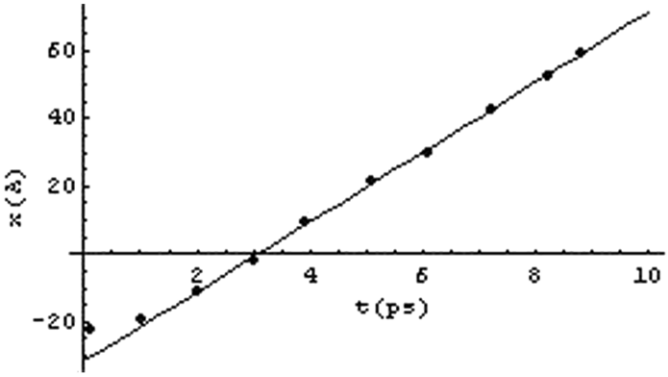

Figure 2. A typical graph of displacement of the crack tip versus simulation time for a crack propagation run with $1.5G_0$ load.

with a very small effect on the energies. The positions of the atoms after every 200 time steps were stored in an output animation file to be used, later on, as input to a graphic engine for the animation of our results. The output file has about 100 frames. In principle, positions of all atom as well as their types could be stored in the animation file. The large storage requirement of animating the whole lattice and the fact that most of the interesting dynamics takes place near the crack region led us to animate only those atoms that are close to the crack region. Therefore, four layers, a total number of about 6400 atoms near the crack region, were employed in each frame.

3. Results and discussions

3.1. Crack propagation in defect free crystal

The crack propagation is studied on a [0 0 1] plane of the fcc nickel crystal. The sample with a starter (0 0 1)[1 0 0] crack system is first strained by an amount that corresponds to the Griffith load $G_0 = 2\gamma_s = 3.76\,\mathrm{J\,m^{-2}}$. Strain ε corresponding to each load G_s is calculated from equation (3) which in turn can be simplified by substituting for $\upsilon = 0.27$ and $E = 317.5 \times 10^9\,\mathrm{J\,m^{-3}}$, $G_s\,(\mathrm{J\,m^{-2}}) = 17.1W\varepsilon^2$, where W is in Angstrom. In the present case, $W = 174$ Å and G_s only depends on the strain, $G_s\,(\mathrm{J\,m^{-2}}) = 2979.4\varepsilon^2$. All the atoms of the slab are displaced, uniformly along the z-direction, by an amount u that is equivalent to the desired strain ε. Then the atoms of the upper and lower most layers are held fixed in the z direction and the forces in the x and y directions are set to zero. The slab is then equilibrated for 20 ps at a fixed temperature of 10 K. Subsequent higher strains are applied to the system on top of the G_0 to produce total loads of $1.2G_0$, $1.5G_0$, $2.0G_0$, $2.5G_0$, $3.0G_0$, $4.0G_0$ and $5.0G_0$. The slab at each load is then equilibrated for 20 ps using the viscous ramping temperature control. The crack-tip position is determined by the inspection of the relative distance between atoms of the upper and lower planes of the crack. Using the graphical engine Xmakemol, one can search for the first broken bond by comparing the separation of pairs of atoms with a value for which the bound is believed to be broken. The crack-tip position determined this way is accurate within one nearest neighbor distance. A plot of crack-tip position versus time for a load of $1.5G_0$ is given in figure 2. The slope of the crack-tip position versus time will become constant after a very short transient time. The velocity of the crack at $1.5G_0$ load is equal to the slope of linear part of figure 2 which is about $1030\,\mathrm{m\,s^{-1}}$.

Table 1. v/v_R versus G_s, where $G_0 = 3.76\,\mathrm{J\,m^{-2}}$, v is the velocity of the crack in $\mathrm{m\,s^{-1}}$ and $v_R = 2797\,\mathrm{m\,s^{-1}}$.

v/v_R	0.283	0.368	0.530	0.594	0.643	0.697	0.727
$G_s\,(\mathrm{J\,m^{-2}})$	$1.2G_0$	$1.5G_0$	$2.0G_0$	$2.5G_0$	$3.0G_0$	$4.0G_0$	$5.0G_0$

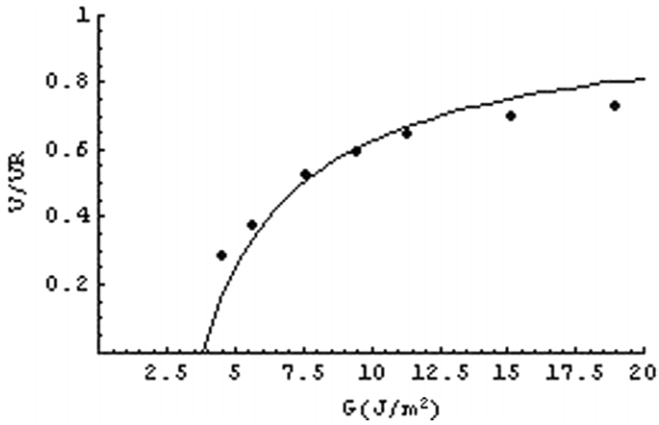

Figure 3. Variation of relative crack speed (v/v_R) with static strain energy release rate G_s from the simulation (points), compared with the continuum prediction (solid line).

Using Rayleigh speed of $v_R = 2797\,\mathrm{m\,s^{-1}}$ a value of 0.368 is obtained for v/v_R for the load of $1.5G_0$.

Steady state velocities of the crack at different loads indicate some interesting features. Between loads G_0 to $1.2G_0$ the crack is stationary and not moving. For loads greater or equal to $1.2G_0$, the crack is moving with a noticeable speed of $792\,\mathrm{m\,s^{-1}}$ which is about 37% of the Rayleigh speed. This suggests that the terminal speed of a brittle crack at low temperature cannot be less than a critical value and there is a forbidden velocity band from zero to the value. This feature is observed in other simulations [17]. Our simulations, at least at the time scale performed here, confirm this feature of brittle crack propagation.

We first calculated the critical value for propagation of the crack by increasing the load on a stationary crack. When we calculated the critical value by ramping down the load on a moving crack, we found our result for G_s was unchanged to an accuracy of $0.1G_0$.

Other loads are applied to the sample and the corresponding v/v_R is calculated for each load and reported in table 1. A graph of v/v_R versus G_s of data from table 1 along with the prediction of continuum fracture mechanics are given in figure 3. By extrapolation of the solid curve in figure 3, a minimum value of $3.76\,\mathrm{J\,m^{-2}}$ is obtained for G_s. This value of G_s is exactly equal to G_0.

The smallest load that caused the crack to propagate is about $G_c = 1.2G_0 = 4.54\,\mathrm{J\,m^{-2}}$. This is obviously different from the corresponding value of the surface energy $G_0 = 2\nu_{(1\,0\,0)} = 3.76\,\mathrm{J\,m^{-2}}$, where $\nu_{(1\,0\,0)} = 1.878\,\mathrm{J\,m^{-2}}$ is the surface energy of the (0 0 1) plane. It should be emphasized that the EAM potential employed here was fitted to a much richer database that includes not only the experimental data but also the first principles data. Specifically, the surface energies $\nu_{(1\,0\,0)}$, $\nu_{(1\,1\,0)}$, and $\nu_{(1\,1\,1\,1)}$ were included in the fitting data. The difference between G_c and G_0 is attributed to the lattice trapping which is in turn a result of the discrete nature of the lattice [18]. The discrete lattice of a crystal generates a periodic potential with

Table 2. Values of ε_c and G_c for crack propagation in presence and or absence of defects. G_c is in unit of $\mathrm{J\,m^{-2}}$. G_{c1} and G_{c2} are defined in the paper.

Configuration	No defects figure 4	Figure 5(*a*)	Figure 5(*b*)	Figure 5(*c*)	Figure 5(*d*)	Figure 5(*e*)
Crack path	Unshifted	Shifted	Shifted	Unshifted	Unshifted	Unshifted
Critical load	$1.2G_0$	$1.6G_0$	$G_{c1} = 1.10G_0$ $G_{c2} = 1.6G_0$	$G_{c1} = 1.10G_0$ $G_{c2} = 1.15G_0$	$G_{c1} = 1.10G_0$ $G_{c2} = 1.15G_0$	$G_{c1} = 1.10G_0$ $G_{c2} = 1.15G_0$

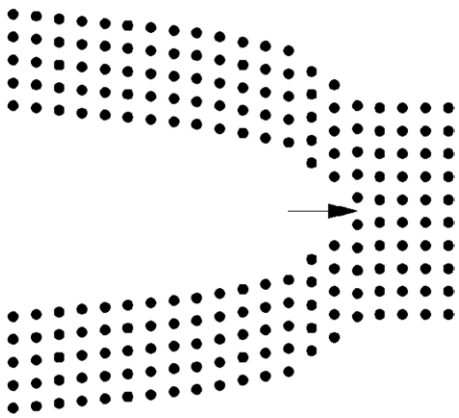

Figure 4. Sketch of the atomic configuration near the crack tip for the lattice with no defects. The arrow represents location of the crack tip.

barriers and wells that a crack needs to overcome to propagate. The heights of the barriers depend on the detail of the interatomic potential model and the lattice structure [18]. A crack could be trapped in these potential wells and, therefore, be arrested even though the applied load is greater than the Griffith load G_0. Using a different EAM Ni potential [19], for exactly the same system size, Gumbsch *et al* [5] obtained a value of $G_c = 1.04G_0$ and, therefore, a smaller lattice trapping.

3.2. *Crack propagation in crystal with defects*

Two lines of vacancies are introduced into the lattice of 160 000 atoms in various positions near the crack tip. Depending on where the lines of vacancies are introduced in the lattice a total of five lattices with defects are constructed (figures 5(*a*)–(*e*)). Each vacancy line is along the crack front (y-direction) and includes four atoms in the computational cell. The two vacancy lines have mirror symmetry with respect to the xy-plane and the lattice with these defects has 159 992 atoms. The corresponding critical values ε_c and G_c were obtained and reported in table 2. The values of G_c are determined to an accuracy of $0.05G_0$. As seen from table 2, G_c for the lattice with defects (G_{cd}) is different from that in the defect-free lattice (G_{c0}). Our calculations indicate that G_{cd} could be greater or smaller than G_{c0} depending on the defect locations in the lattice. If lines of vacancies are introduced in locations shown as empty circles in figures 5(*a*) and (*b*), then $G_{cd} > G_{c0}$. In addition, the crack shifts up or down a layer as they propagate beyond the defects. If lines of vacancies are introduced in locations shown as empty circles in figures 5(*c*), (*d*), and (*e*), then $G_{cd} < G_{c0}$. In figures 5(*b*)–(*e*), there are two Gs, G_{c1} and G_{c2}. The former (G_{c1})

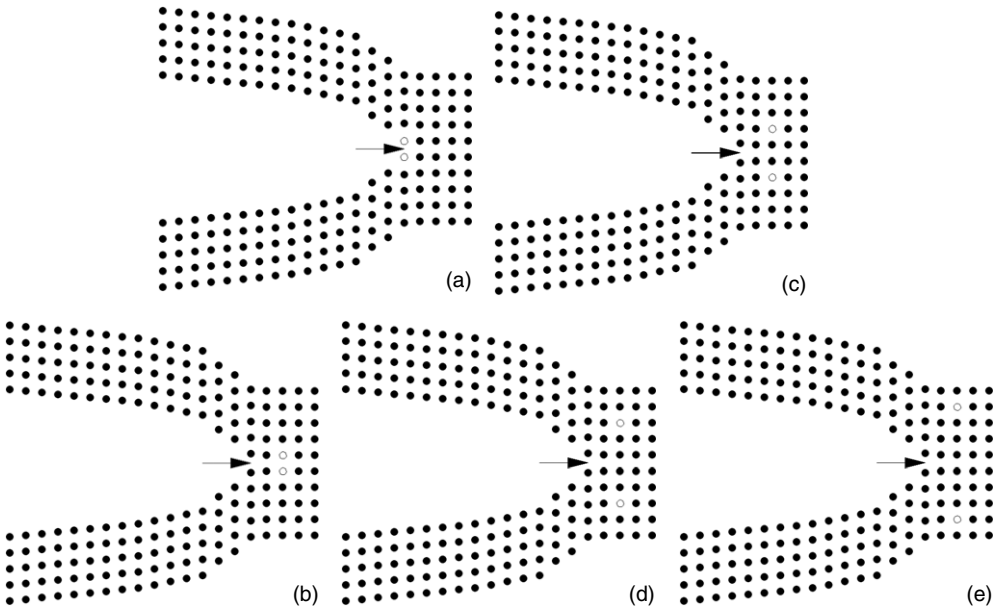

Figure 5. Sketches of the atomic configurations near the crack tip for the lattices with defects. Two lines of vacancies are introduced along the crack front (y-axis) in a symmetric fashion. The lines of vacancies are indicated as open circles. The arrow represents location of the crack tip.

represents the critical value of G for the starter crack tip to propagate to the plane containing the vacancy lines. The latter (G_{c2}) is the corresponding value for the crack tip at the location of the vacancy lines to propagate further. Our calculations indicate that $G_{c1} < G_{c2}$. In configurations 5(c)–(e) the crack continues along the original crack axis as it passes the defects.

In order to better understand the defect results for G, we examine the strain energy near the crack tip with $G < G_c$ for both the defect-free lattice and the lattices with lines of vacancies. The lattice without defects is relaxed and the potential energy of atom i, E_{1i}, is calculated. The lattice without defects is loaded to $1.1G_0$ (3.66% strain), and the relaxed energy of atom i, E_{2i}, is calculated using energy minimization. The strain corresponding to $1.1G_0$ is applied to the atoms of the upper and lowermost layers in small increments. This adiabatic way of straining the system is important for the minimization procedure to converge faster. The strain energy of atom i, $\Delta E_i = E_{2i} - E_{1i}$, is the change in potential energy of atom i due to the applied strain. Similarly, calculations are performed for the lattices with two vacancy lines and a load of $1.1G_0$. A graph of the strain energy per atom ΔE_i as a function of layer number along the crack (in the x-direction) for each defect lattice is plotted in figures 6(a)–(d). For comparison, the strain energy along the crack of the defect-free lattice is plotted in each figure. Even though this load is less than the critical load for the propagation of the crack, an examination of the strain energy distribution can explain the observed fracture behaviour. In figure 6(a) the peak in the strain energy is shifted away from the original crack tip position at atom layer 7 to layer 8 and reduced in magnitude. Thus, the two vacancy lines at the crack tip in the configuration in figure 5(a) have effectively formed a new blunted crack tip. This indicates that a larger strain than was needed in the defect-free lattice will be needed to produce the strain field at the crack tip necessary to break the bond and advance the crack. In figure 6(b) we see a different effect. Here the lines of vacancies are out in front of the crack tip and they produce an enhancement

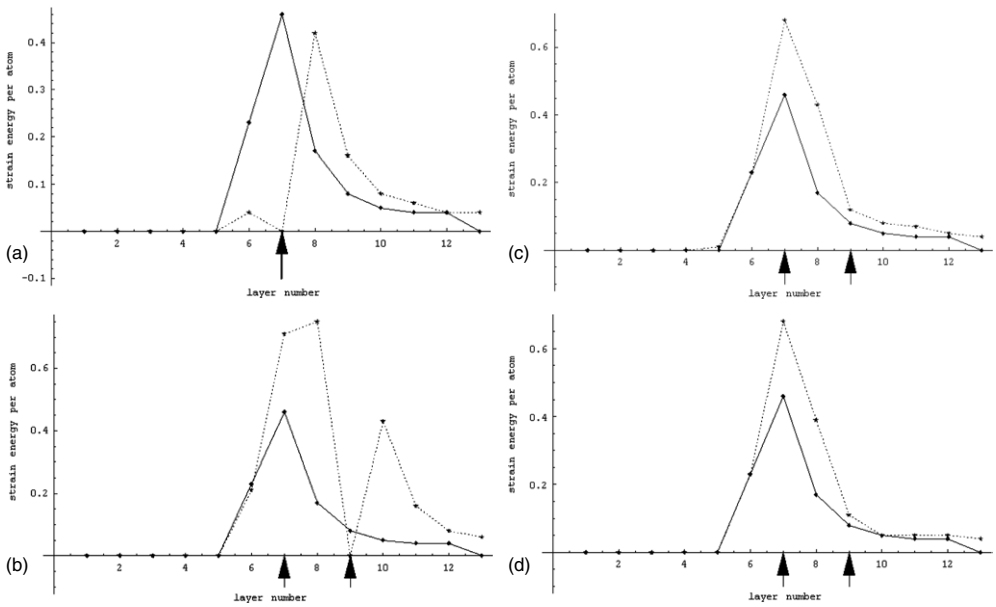

Figure 6. Strain energy per atom for the defect-free configuration in figure 4 and the configurations with defects in figures 5(*a*)–(*d*) with a load of $1.1G_0$. In each graph, the solid line plus diamond is the strain energy per atom for the lattice with no defects and the dashed line plus star are the corresponding graphs for the lattices with defects. Figures 6(*a*)–(*d*) correspond to the configurations in figures 5(*a*)–(*d*), respectively. First arrow at layer 7 represents the location of the crack tip. The second arrow represents the location of the vacancy lines.

in the strain energy at the crack tip over the defect-free case. This indicates that a strain energy at the crack tip sufficient to propagate the crack can be achieved with a lower applied strain than was needed in the defect free lattice. When the crack reaches the plane containing the pair of vacancy lines, it will be identical to the configuration in 5(*a*). Now the larger G_c corresponding to this configuration will be needed to advance the crack. The pair of adjacent vacancies merge with the crack tip to form a blunted tip. When the crack continues to propagate from this blunted tip, it shifts one lattice space while continuing in the same [1 0 0] direction. For both configurations 5(*c*) and (*d*) with the pair of vacancies symmetrically displaced from the crack axis, the plots in 6(*c*) and (*d*) show that the strain energy at the crack tip is enhanced over the defect-free case. Therefore, a lower applied strain will initiate crack propagation in these defective lattices than in the defect-free lattice. G_c increases as the crack tip approaches the defects, but remains slightly less than in the defect-free lattice due the enhancement effect on the strain at the crack tip by the vacancies.

For the configurations studied, the defects tend to promote crack propagation towards them. Note these defect configurations are all symmetrical about the crack axis, so the crack actually propagates towards the symmetry point between the defects. If the crack runs into the vacancies, it is blunted and a larger strain will be needed to be applied to propagate the crack. This demonstrates the ability of these defects to retard crack propagation. However, the separated vacancy lines lower G_c showing a behaviour similar to a weakening of the strength of the material. This effective weakening in material strength is consistent with the results of two papers given in [12]. Both papers in [12] give statistical studies of cracking in the presence of random distributions of vacancy and Frenkel defects in copper and α-Fe single crystals, respectively.

4. Conclusions

MD simulations using the EAM were conducted to investigate brittle fracture under mode I loading in a Ni single crystal in the presence of vacancies. The crack system (0 0 1)[1 0 0] in a slab of 160 000 atoms was studied. First, the fracture properties of the defect free system were investigated. Then defects consisting of lines of vacancies were introduced in various positions near the crack tip. For both systems, the critical loads and strain energy distributions around the crack tip were investigated. By examining the change in strain energy for each atom in the region around the crack tip and defects, one can better understand how defects alter the fracture process.

For the Ni system studied, the vacancy lines were shown to enhance strain fields at the crack tip, resulting in lower critical strain energy release rates than in defect-free crystals. Thus, the effect was to weaken the material. However, when the crack tip merged with the vacancy lines the crack tips became blunted, reducing the strain energy at the tip and effectively toughening the material to fracture. Depending on the placement of the defects and the path of the crack, the material could be either weakened or toughened to fracture.

Acknowledgments

This research was supported in part by the Applied Mathematical Sciences Research Program of the Office of Advanced Scientific Computing Research, the US Department of Energy, under contract DE-ACO5-00OR22725 to TK. Technical supports of Professors Rick Adkins and Ed. Donley of the mathematics department, here at IUP, are greatly appreciated. The authors are grateful to Oak Ridge National Laboratory for computational resources.

References

[1] Sieradzki K, Dienes G J, Paskin A and Massoumzadeh B 1998 *Acta. Metall.* **36** 651
Rafii-Tabar H 2000 *Phys. Rep.* **325** 239
Zhang Y W, Wang T C and Tang Q H 1995 *Scr. Metall. Mater.* **33** 267
[2] Keller R R, Phelps J M and Read D T 1996 *Mater. Sci. Eng.* A **214** 42
Hu Y M and Wang Z G 1996 *Scr. Mater.* **35** 1019
[3] Daw M S and Baskes M I 1983 *Phys. Rev. Lett.* **50** 1285
Daw M S and Baskes M I 1984 *Phys. Rev.* B **29** 6443
Baskes M I 1992 *Phys. Rev.* B **46** 2727
[4] Mishin Y, Farkas D, Mehl M J and Popaconstantopoulos D A 1999 *Phys. Rev.* B **59** 3393
[5] Gumbsch P, Zhou S J and Holian B L 1997 *Phys. Rev.* B **55** 3445
Gumbsh P 1995 *J. Mater. Res.* **10** 2897
[6] Marder M P 2000 *Condensed Matter Physics* (New York: Wiley)
Hauch J A, Holland D, Marder M P and Swinney H L 1999 *Phys. Rev. Lett.* **82** 3823
[7] Freund L B 1972 *J. Mech. Phys. Solids* **20** 129
Freund L B 1972 *J. Appl. Mech.* **31** 1027
Freund L B 1990 *Dynamic Fracture Mechanics* (Cambridge, UK: Cambridge University Press)
[8] Swadener J G, Baskes M I and Nastasi M 2002 *Phys. Rev. Lett.* **89** 85503
[9] Musgrave M J P 1959 *Rep. Prog. Phys.* **22** 74–96
[10] Wolfram S 1999 *The Mathematica Book* 4th ed (Champaign, IL/New York: Wolfram Media/Cambridge University Press)
[11] Schroder C T and Scott W R 2001 *J. Acoust. Soc. Am.* **110** 2867
[12] Heino P, Hakkinen H and Kaski K 1998 *Phys. Rev.* B **58** 641
Saraev D, Kizler P and Schmauder S 1999 *Modelling Simul. Mater. Sci. Eng.* **7** 1013
[13] Nordseick A 1962 *Math. Comput.* **16** 22
[14] Alan M P and Tildesley D J 1987 *Computer Simulations of Liquids* (Oxford, UK: Oxford University Press)
[15] Finnis M W, Agnew P and Foreman J E 1991 *Phys. Rev.* B **44** 567

[16] Mandl F 1987 *Statistical Physics* 2nd ed (New York: Wiley)
[17] Holland D and Marder M P 1998 *Phys. Rev. Lett.* **80** 746
Holland D and Marder M P 1998 *Phys. Rev. Lett.* **81** 4029
[18] Thomson R, Hsieh C and Rana V 1971 *J. Appl. Phys.* **42** 3154
Curtin W A 1990 *J. Mater. Res.* **5** 1549
[19] Foiles S M, Baskes M I and Daw M S 1986 *Phys. Rev.* B **33** 7983